

THEORETICAL INSIGHTS TO
SYMMETRY-INDUCED SPIN SPLITTINGS
AND TEXTURES IN (NON)-MAGNETIC
MATERIALS

SAJJAN



DEPARTMENT OF PHYSICS
INDIAN INSTITUTE OF TECHNOLOGY DELHI
JULY 2024

© Indian Institute of Technology Delhi (IITD), New Delhi, 2024

**THEORETICAL INSIGHTS TO
SYMMETRY-INDUCED SPIN SPLITTINGS
AND TEXTURES IN (NON)-MAGNETIC
MATERIALS**

by

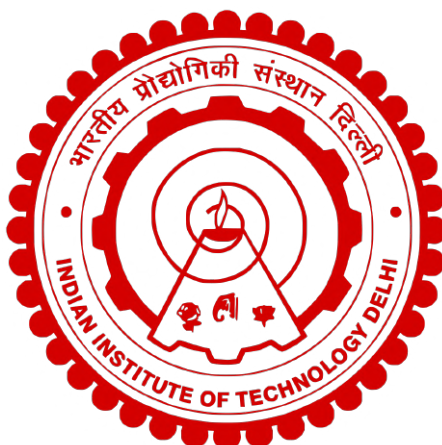
SAJJAN

Department of Physics

Submitted

in fulfillment of requirements of degree of Doctor of Philosophy

to the



INDIAN INSTITUTE OF TECHNOLOGY DELHI

JULY 2024

Dedicated to loving memories of my father

Certificate

This is to certify that the thesis entitled “**Theoretical Insights to Symmetry-Induced Spin Splittings and Textures in (Non)-Magnetic Materials**” being submitted by **Sajjan**, to the Indian Institute of Technology Delhi, for the award of the degree of **Doctor of Philosophy** in Physics is a record of bonafide research work carried out by him under my supervision and guidance. He has fulfilled the requirements for the submission of the thesis, which to the best of my knowledge has reached the required standard. The material contained in the thesis has not been submitted in part or full to any other University or Institute for the award of any degree or diploma.

Prof. Saswata Bhattacharya

Thesis Supervisor

Department of Physics,

Indian Institute of Technology Delhi,

Hauz Khas, New Delhi 110016, India.

Date:.....

Place: New Delhi

Acknowledgments

I extend my deepest gratitude to my Ph.D. supervisor, Prof. Saswata Bhattacharya. Every interaction with him has been a learning experience, contributing significantly to my professional and personal development. His expertise, encouragement, and constructive feedback have been instrumental in shaping the direction of this thesis. His invaluable advice, insightful comments, novel ideas, and dedicated research guidance have served as the cornerstone of my development as both a student and an independent research scholar. Thank you Sir!

I am thankful to members of my student research committee: Prof. Hemant K Kashyap, Prof. Sankalpa Ghosh, and Prof. Rohit Narula for their expertise and thoughtful insights that have significantly enriched the quality of my research. I am deeply grateful to my M.Sc. project supervisor, Prof. Ravinder R. Puri, for initially sparking my interest in theoretical physics and cultivating my critical thinking skills.

A special acknowledgment goes to my DISCERE group members: Dr. Sikha Saini, Dr. Pooja Basera, Dr. Manish Kumar, Dr. Arunima Singh, Dr. Deepika Gill, Dr. Manjari Jain, Dr. Preeti Bhumla, Ankita Phutela, Sanchi Monga, Ruman Moulik, Riya Gupta, Shantanu Pathak, and Divyanshi Tyagi. Your collaborative spirit, diverse perspectives, and intellectually stimulating environment have positively impacted this research.

I want to thank our collaborators at IIT Mandi: Prof. Venkata Krishnan, Dr. Ashish Kumar, and Devendra Sharma for great discussions on the catalysis project.

I am deeply thankful to IIT Delhi and CSIR for providing me the facilities and funding to carry out this research and present it at international conferences. I am truly indebted to Navodaya Vidyalaya Samiti for supporting my education up to the senior secondary.

Finally, I thank *my parents, family, and friends* who have always been there for me.

Sajjan Sheoran

Abstract

Spin splittings and associated spin textures play a pivotal role in spintronics application (e.g., charge-to-spin conversion). The role of crystal symmetries in determining spin polarization through spin-orbit coupling (SOC) is established in pioneer works by Dresselhaus and Rashba. Nevertheless, the practical use of these materials in spin transport is constrained by the SOC-induced spin dephasing mechanisms. In addition, the toxicity, rarity, and instabilities of materials containing heavy atoms are also challenging. The materials with uniform spin configurations in the momentum space, termed as persistent spin texture (PST), provide nondephasing spin transport. However, PSTs observed in the regime of linear (in \mathbf{k}) splitting and exist locally in Brillouin zone (BZ).

Here, we report first-principles density functional theory simulation and symmetry-based $\mathbf{k}\cdot\mathbf{p}$ analysis to obtain novel spin-splitting mechanisms with nontrivial spin textures in magnetic and nonmagnetic crystalline materials. We demonstrate full-plane PSTs in the regime of purely cubic spin splitting protected by the in-plane mirror and threefold rotation symmetries. A large class of experimentally synthesized bulk materials shows cubic-ordered PSTs with D_{3h} and C_{3h} point group symmetries. Moreover, σ_h symmetry enforces the spin textures of two-dimensional (2D) materials to the out-of-plane direction in the entire BZ. Our calculations demonstrate that it is local site symmetries that determine the nature of spin splittings and PSTs.

Structural symmetry can be varied using external perturbations, i.e., electric and strain fields, to modulate the spin and valley physics in 2D materials. By performing DFT calculations on monolayer MSi_2N_4 (M=Mo, W), a prototypical septuple atomic layered two-dimensional material, we demonstrated that Rashba splitting can be induced by breaking the σ_h through an out-of-plane external electric field and chemical substitution of elements (*Janusization*). The low energy electron and hole valleys drift far off the K/K' point under uniaxial strains. The direction and strength of valley drift strongly depend on the nature of the charge carrier and uniaxial strain with a more substantial response along the zigzag path. The changing geometric

properties of Bloch states affect the Berry curvatures and circular dichroism. Specifically, Berry curvature dipole is significantly enhanced under the tensile strain along armchair and zigzag directions. Meanwhile, the particle-hole asymmetry arising from nonequivalent electron and hole valley drifts relaxes the selection rules, thus reducing the degree of circular polarization up to ~ 0.98 . Therefore, strain engineering of valley physics in the monolayer MSi_2N_4 is of prime importance for valleytronics.

Recently, antiferromagnetic (AFM) materials have emerged as viable substitutes for non-magnetic and ferromagnetic materials, benefiting from resilience towards stray fields, ultrafast dynamics, magnetotransport effects, and lack of susceptibility to magnetic perturbations. Centrosymmetric antiferromagnetic semiconductors, although abundant in nature, appear less favorable in spintronics owing to the lack of inherent spin polarization and magnetization. We unveil hidden Zeeman-type nonrelativistic spin splitting (NRSS) in layered centrosymmetric antiferromagnets with asymmetric sublayer structures through first-principles simulations and symmetry analysis. In addition, we demonstrate a paradigm to harness NRSS by twisting the bilayer of centrosymmetric antiferromagnets with commensurate twist angles. We observe spin-momentum locking by first-principles simulations and symmetry analysis on prototypical MnPSe_3 and MnSe antiferromagnets. The strength of NRSS (up to $80 \text{ meV}\text{\AA}$) induced by twisting is comparable to SOC-induced linear Rashba-Dresselhaus effects. The results also demonstrate how applying biaxial strain and a vertical electric field tune the NRSS. The design principle to obtain Zeeman-type splitting in centrosymmetric antiferromagnets established here expands the range of materials to look for spintronics.

स्पिन स्प्लिटिंग और संबंधित स्पिन टेक्सचर्स, अर्थात मोमेंटम स्थान में स्पिन पॉलराइजेशन वेक्टर्स का वितरण, स्पिनट्रॉनिक्स अनुप्रयोग (उदा., चार्ज-टू-स्पिन कनवर्जन) में महत्वपूर्ण भूमिका निभाते हैं। क्रिस्टल सममितियों की भूमिका, जिनका संबंध स्पिन-ऑर्बिट कप्लिंग (SOC) के माध्यम से स्पिन पॉलराइजेशन का निर्धारण करने में है, इसे ड्रेसलहांस और राशबा द्वारा किए गए प्रमुख कार्यों में स्थापित हो गई है। हालांकि, इन सामग्रियों का वाणिज्यिक उपयोग स्पिन परिवहन में स्पिन-ऑर्बिट कप्लिंग (SOC) के कारण होने वाले स्पिन डीफेजिंग प्रक्रियाओं से सीमित है, अर्थात एलियट-याफेट स्पिन रिलैक्सेशन और ड्याकोनोव-पेरेल स्पिन डीफेजिंग। इसके अलावा, भारी परमाणु अणुओं को शामिल करने वाली सामग्रियों की विषाक्तता, दुर्लभता, और अस्थिरताओं की चुनौतियाँ भी हैं। मोमेंटम स्थान में एक समरूप स्पिन विन्यास को बनाए रखने वाली सामग्रियाँ, जिसे स्थिर स्पिन टेक्सचर (PST) कहा जाता है, स्थिर स्पिन-हेलिक्स मैकेनिज्म के माध्यम से दीर्घकालीन कैरियर स्पिन जीवनकाल प्रदान करती हैं। हालांकि, अब तक अध्ययन की गई अधिकांश PSTs को k में रूपरेखा की गई स्प्लिटिंग का श्रेय दिया गया है और ये विशिष्ट उच्च-समरूपता बिंदुओं के आस-पास स्थानीय रूप से अस्तित्वहीन हो जाती हैं ब्रिल्वॉ क्षेत्र (BZ) के।

यहाँ, हम पहले-सिद्धांत सिमुलेशन और सिमेट्री-आधारित $k \cdot p$ विश्लेषण का उपयोग करते हैं ताकि चुंबकीय और अचुंबकीय द्रव्यमानों में असामान्य स्पिन टेक्सचर्स के साथ नए स्पिन-स्प्लिटिंग मैकेनिज्म प्राप्त किए जा सकें। हम पूरी-तल PSTs की प्रकृति की रिपोर्ट करते हैं जो केवल क्यूबिक स्पिन स्प्लिटिंग क्षेत्र में पूरी तरह से बनाए जा रहे हैं, जिसे इन-प्लेन मिरर (σ_h) और तिनमुखी घूमन (C_3) द्वारा प्रबल किया जाता है। एक बड़े श्रेणी का प्रयोगशाला संश्लेषित बल्क सामग्रियों में D_{3h} और C_{3h} बिंदु समूह सममितियाँ दिखाती हैं। इसके अलावा, σ_h सममिति दो-आयामी (2D) सामग्रियों की स्पिन टेक्सचर्स को पूरी BZ में बाहरी-प्लेन दिशा में अनुबद्ध करती है। हमारी गणनाएँ दिखाती हैं कि यह स्थानीय स्थान सममितियाँ हैं जो स्पिन स्प्लिटिंग्स और PSTs की प्रकृति का निर्धारण करती हैं।

संरचनात्मक सममिति को विभिन्न कार्यात्मक प्रभावों का सामना करने के लिए बदला जा सकता है, उदाहरण के लिए, इलेक्ट्रिक और तनाव क्षेत्रों का उपयोग करके 2D सामग्रियों में स्पिन और वैली भौतिकी को सम्मोदित करने के लिए। मोनोलेयर MSi_2N_4 ($M=Mo, W$) पर घनत्व कार्यात्मक सिद्धांत (DFT) गणनाएँ करके, एक उदाहरणीय सप्तांश आणविक स्तर की 2D सामग्री, σ_h को ब्रेक करके बाहरी इलेक्ट्रिक फील्ड और तत्त्वों के रूप में उपयोग से राशबा स्प्लिटिंग प्रेरित किया जा सकता है। कम ऊर्जा इलेक्ट्रॉन और होल वैली टिरों केन्द्रित स्ट्रेन के तहत K/K' बिंदु के बहुआक्षरी दबाव के तहत दूर चला जाता है। वैली चलन की दिशा और ताकत का प्रतिकूल उत्तर चिरपथ के साथ अधिक स्थिर प्रतिक्रिया के साथ, आधारित है। हमारे फिंडिंग्स, सूक्ष्मक कक्षय योगदान और सममिति कमी की महत्वपूर्ण भूमिका को प्रदर्शित करते हैं। ब्लोच स्थितियों की बदलती रूपरेखा बेरी कर्वेचर्स और सर्कुलर डाइक्रोइज्म को प्रभावित करती हैं। विशेष रूप से, आर्मचेयर और जिगजैग दिशाओं के साथ तनाव स्थिति के तहत बेरी कर्वेचर डाइपोल सांग्राता को सुधारा जाता है। इसके बीच, गैरसमरूप इलेक्ट्रॉन और होल वैली चलन से उत्पन्न धारापूर्व असममिति नियमों को

धीरे-धीरे शांत करती है, जिससे चिरपथीकरण की दिशा में साइक्लर पोलराइजेशन की डिग्री को ~ 0.98 तक कम करती है। इसलिए, मोनोलेयर MSi_2N_4 में वैली भौतिकी के तनाव का इंजनियरिंग करना वैलीट्रॉनिक्स के लिए प्रधान महत्वपूर्ण है।

हाल ही में, एंटीफेरोमैग्नेटिक (AFM) सामग्रियाँ गैरचुंबकीय और फेरोमैग्नेटिक सामग्रियों के लिए व्यावसायिक विकल्प के रूप में प्रकट हो रही हैं, जो बिखरे क्षेत्रों, अल्ट्राफास्ट गतिविधि, मैग्नेटोट्रांसपोर्ट प्रभावों, और चुंबकीय उत्तेजनों के प्रति सहिष्णुता के लाभान्वित हो रही हैं। सेंट्रोसाइमेट्रिक एंटीफेरोमैग्नेटिक सेमीकंडक्टर्स, हालांकि प्राकृतिक रूप से प्रचुर हैं, स्वाभाविक रूप से स्पिन पोलराइजेशन और मैग्नेटाइजेशन की कमी के कारण स्पिनट्रॉनिक्स में कम पसंदीदा लगते हैं। हम लयरड सेंट्रोसाइमेट्रिक एंटीफेरोमैग्नेट्स में एसीमेट्रिक सबलेयर संरचनाओं के माध्यम से छिपे जीमेन-प्रकार के गैर सांवेधानिक स्पिन स्प्लिटिंग (NRSS) का खुलासा करते हैं, पहले-सिद्धांत सिमुलेशन और सिमेट्री विश्लेषण के माध्यम से। हाल ही में सिंथेसाइज़ किए गए मोनोलेयर MnSe के दो-तहती संरूप में, हम दिखाते हैं कि विशिष्ट k बिंदुओं के आस-पास समकक्ष उपतलों पर स्थानीय रूप से विभाजित अवस्थाएँ \mathcal{PT} -सममित पैयर्स बनाती हैं। और अधिक महत्वपूर्ण है, हम \mathcal{PT} -सममित एंटीफेरोमैग्नेट्स की दो-तहती को घुमाने के द्वारा NRSS का उपयोग करते हैं। प्रोटोटाइप MnSe और MnPSe_3 पर DFT सिमुलेशन करके, हम पूर्वानुमान करते हैं कि ब्रिल्युइन जोन के विशिष्ट पथों पर राशबा-ड्रेसेलहॉस और जीमेन-प्रकार NRSS उत्पन्न हो सकते हैं। घुमाने के द्वारा उत्पन्न राशबा-ड्रेसेलहॉस स्पिन स्प्लिटिंग की ताकत ($\sim 90 \text{ meV}\text{\AA}$) स्पिन-या-बाधित स्थिति की तुलना में है। परिणाम यह भी दिखाते हैं कि दो-सेंट्रिक तनाव और एक सीधी विद्युत क्षेत्र लागू करने से NRSS के मात्रा को स्वरूपित करने की संभावना है। यहाँ सेंट्रोसाइमेट्रिक एंटीफेरो मैग्नेट्स में जीमेन-प्रकार स्प्लिटिंग प्राप्त करने के लिए डिज़ाइन सिद्धांत विस्तार करता है और स्पिनट्रॉनिक्स के लिए सामग्रियों की खोज की सीमा को बढ़ाता है।

Contents

Certificate	i
Acknowledgements	ii
Abstract	iii
List of Figures	xi
List of Tables	xxi
1 Introduction	1
1.1 Materials	1
1.2 Spintronics	2
1.3 Symmetries in condensed matter	3
1.4 Spin splittings	4
1.5 Spin-valley coupling	6
1.6 Nonrelativistic spin-moment coupling in antiferromagnets	7
1.7 Motivation of this thesis	10
1.8 Organization of this thesis	11
2 Modeling electronic structure: Density functional and $k.p$ perturbation theory	14
2.1 Background	14
2.2 Many-body physics: A theoretical framework	14
2.3 Density functional theory	17
2.3.1 Hohenberg-Kohn formalism	18
2.3.2 Kohn-Sham ansatz	19
2.3.3 Exchange and correlation Energy	22

2.3.4	Spin-Polarized DFT	23
2.3.5	SOC in DFT	25
2.3.6	Basis set	27
2.3.7	Pseudopotentials	30
2.3.8	Projector augmented-wave method	33
2.3.9	Computational methods	34
2.4	<i>k.p</i> perturbation theory with SOC	35
2.4.1	Method of invariants	37
3	Linear Rashba-Dresselhaus effects in perovskite oxides and chalcogenides	40
3.1	Introduction	40
3.2	Rashba spin splitting in bulk perovskite KIO_3	42
3.2.1	Structural and ferroelectric properties	43
3.2.2	Electronic properties and spin splitting effects	44
3.3	Rashba-Dresselhaus spin splittings in chalcogenides	52
3.3.1	Crystal and electronic Structures	54
3.3.2	Spin splitting analysis	55
3.4	Summary and outlook	59
4	Symmetry-protected persistent spin textures in full-zone and full-plane with cubic splittings	61
4.1	Introduction	61
4.2	Cubic-ordered full-plane PSTs in hexagonal bulk materials	62
4.2.1	Symmetry analysis and electronic band structures	63
4.2.2	Spin splitting and effective <i>k.p</i> Hamiltonian	65
4.3	Coupled spin-valley physics and full-zone PSTs in 2D WSi_2N_4 family	72
4.3.1	Crystal structures and stability	74
4.3.2	Electronic structure	77
4.3.3	Full-zone PST	78
4.3.4	Hidden full-zone PST	83
4.4	Summary and outlook	85
5	Reducing symmetry to modulate spin and valley physics in 2D materials	87
5.1	Introduction	87

5.2	Symmetry control of spin-valley physics in 2D Janus WSiGeZ_4	89
5.2.1	Crystal structure and electronic properties	90
5.2.2	Valley physics	91
5.2.3	Berry curvature modulation	97
5.2.4	Rashba effect	99
5.2.5	The role of electric field	103
5.2.6	Carrier mobility	103
5.3	Probing the uniaxial strain-dependent valley drift and Berry curvature in mono- layer MoSi_2N_4	104
5.3.1	Lattice under strain	104
5.3.2	Monolayer MoSi_2N_4	107
5.3.3	Valley drifts	108
5.3.4	Berry curvature modulation	112
5.3.5	Circular dichroism under strain	113
5.4	Summary and outlook	115
6	Nonrelativistic spin splittings from 2D \mathcal{PT}-symmetric antiferromagnets	117
6.1	Introduction	117
6.2	Hidden Zeeman-type spin splittings	118
6.2.1	Monolayer MnSe	118
6.2.2	Bilayer stackings	119
6.2.3	Symmetry analysis	120
6.2.4	DFT analysis	122
6.3	Spin splittings in twisted bilayers	127
6.3.1	Monolayer MnSe and MnPSe_3	127
6.3.2	Twisted bilayer MnSe and MnPSe_3	129
6.3.3	Nonrelativistic Rashba-Dresselhaus-like spin splittings	130
6.3.4	Materials classification	132
6.3.5	Effect of external electric field and biaxial strain	133
6.4	Summary and outlook	135
7	Epilogue and outlook	136

Curriculum vitae

List of Figures

1.1	Graphical abstract for spins and related effects. This Figure is taken from Ref. [1].	3
1.2	Splitting of d orbitals under octahedral and tetragonal crystal fields.	3
1.3	(a) Linearly dispersed bands and associated spin configurations in momentum space for (b) linear Rashba, (c) linear Dresselhaus, and (d) persistent spin texture cases.	5
1.4	Schematic illustration of spin-valley coupling in 2D hexagonal materials. The spin polarization at the time-reversal conjugate points K and K' is opposite in nature.	6
1.5	This Figure is taken from Ref. [2] © Copyright 2021 American Physical Society. Classification of spin splittings prototypes (SSTs) based on the magnetic ordering and present symmetries. Here, θ , I , and T represent time-reversal, inversion and translation operation, respectively. Note that the notation we followed may differ from the one used in this Figure and will be specified whenever required.	9
2.1	The mapping of interacting system's to a auxiliary non-interacting system with the same ground-state electron density.	20
2.2	Self-consistent scheme to solve the KS equations.	21
2.3	Schematic illustration of pseudopotential approach. The all-electron wavefunction associated with Coulomb potential is shown by red lines. The pseudo wavefunction consistent with pseudopotential is shown by blue dashes.	31
3.1	Crystal structure of KIO_3 in the (a)-(b) $R3m$ phase and (c)-(d) $R3c$ phase. The violet, orange and red balls denote the K, I and O ions, respectively.	42
3.2	Band structure and PDOS for $R3m$ phase calculated using PBE (a) without SOC and (b) with SOC. Here, inset shows the first BZ for the hexagonal phase.	44

- 3.3 (a) VBs and (b) CBs of KIO for $R3m$ phase with SOC along A-L line (energy vs k_x). Here black solid lines and red dashed lines are obtained by DFT and parametrization of the model, respectively. (c)-(d) Spin textures of two upper most VBs and (e)-(f) two lowest CBs. The arrows and color projection represent the in-plane (x, y) and out-of-plane (z) components of texture with respect to the (k_x - k_y) plane. 46
- 3.4 Band structure and PDOS for $R3c$ phase calculated using PBE (a) without SOC and (b) with SOC. 48
- 3.5 (a) VBs and (b) CBs of KIO for $R3c$ phase with SOC along Γ -M line (energy vs k_x). (c) Lowest four CBs around the k -point A with the full model given in Eq. 3.6 and (d) with modified model excluding the terms containing the orbital DOF (obtained using $\eta = \xi = \Delta = \Lambda = K = \rho = 0$ in Eq. 3.6). Here, black solid lines and red dashed lines are obtained by DFT and parametrization of the models, respectively. Spin textures of (e)-(f) two lowest CBs, (g)-(h) two uppermost VBs around k -point Γ and (i)-(l) lowest four CBs around k -point A. The arrows and color projection represent the (S_x, S_y) and S_z components of spin texture with respect to the (k_x - k_y) plane. Our spin textures are prepared using convention [(i)-(l) as examples] that if at (k_x, k_y) point, energy eigenvalues associated with (i), (j), (k) and (l) are $e_{1k}, e_{2k}, e_{3k}, e_{4k}$, respectively, then $e_{1k} \leq e_{2k} \leq e_{3k} \leq e_{4k}$ 49
- 3.6 (a) Band gap (E_g), (b) Rashba spin splitting energy(δE) and (c) Rashba coefficients (α_R) as a function of strain (ϵ). The A^1 and A^2 show the information about splitting around k -point A in $R3m$ phase around the CBM and VBM, respectively. In the same manner, Γ^1 and Γ^2 show splitting in $R3c$ phase around k -point Γ 51
- 3.7 Schematic crystal structure of orthorhombic $\text{Sn}_2\text{SbX}_2\text{I}_3$ ($X = \text{S}, \text{Se}$) in (a) $Cmc2_1$ phase and (b) $Cmcm$ phase. Electronic band structure and partial density of states (pDOS) of (c) $\text{Sn}_2\text{SbS}_2\text{I}_3$ in $Cmc2_1$ phase, (d) $\text{Sn}_2\text{SbS}_2\text{I}_3$ in $Cmcm$ phase, and (e) $\text{Sn}_2\text{SbSe}_2\text{I}_3$ in $Cmc2_1$ phase using PBE+SOC. 55

- 3.8 (a)-(b) VBs and (c)-(d) CBs of $\text{Sn}_2\text{SbS}_2\text{I}_3$ along k_x and k_y directions. The black lines and red dots are bands obtained using DFT and $\mathbf{k}\cdot\mathbf{p}$ model, respectively. Spin textures of (e),(g) two highest VBs, and (f),(h) two lowest CBs, computed using DFT. (i)-(l) are model-resulted spin textures, counterparts of (e)-(h). The arrows denote the in-plane (S_x, S_y) components of spin. The S_z component is zero in the considered range. 57
- 4.1 (a) Schematic illustration of band structure due to purely cubic spin splitting. Here, the band energies $E_{\mathbf{k}}$ vary with \mathbf{k} in the form, $E_{\mathbf{k}} = \alpha k^2 \pm \eta k^3$. (b) Schematic PST due to cubic spin splittings. The color represents the out-of-plane (z -) component of spin textures (note that in-plane (x -, y -) spin components are zero). Here, the red and blue colors denote the spins in the state $|\uparrow\rangle$ and $|\downarrow\rangle$, respectively. Here, $|\uparrow\rangle$ and $|\downarrow\rangle$ are the eigenstates of σ_z with eigenvalues $+1$ and -1 , respectively. Θ is the angular difference between line separating the sectors with eigenvalues $+1$ and -1 , and $k_y = 0$. (c) First BZ of the hexagonal structure. Blue lines highlight the path used for band structure calculation. (d) BZ of the hexagonal structure within the $(k_x - k_y)$ plane, where k_x and k_y are the cartesian reciprocal lattice vectors. The lattice vectors are denoted by a and b , whereas the reciprocal ones are represented by a^* and b^* , respectively. The symmetry elements (C_{3z} , M_{xy} and M_{xz}) of the D_{3h} point group are also shown. The black solid dot and dashed lines represent the rotation axis and mirror planes, respectively. 63

- 4.2 (a) Calculated phonon dispersion for $\text{K}_3\text{Ta}_3\text{B}_2\text{O}_{12}$. (b) Spin-resolved band structures along high-symmetry-path are shown. The color bar indicates the expectation values of the S_x , S_y and S_z spin components. (c) The calculated spin-resolved band structure of lower CBs along the path $\text{K}-\text{M}-\Gamma$. (d) Spin texture of lower CB around the M point in $k_z = 0$ plane. Note that there should be two spin-textures associated with two bands. Here, the only one branch associated with the outer band is shown. The inner branch has an opposite spin orientation with respect to outer branch at every (k_x, k_y) point. The spin resolved band structures around (e) Γ point (along $\text{M}-\Gamma-\text{M}$) and (f) A point (along $\text{L}-\text{A}-\text{L}$). The k -point (k_x, k_y) ranges considered to compute the band structure and spin textures around the high symmetry point are indicated in the units of reciprocal lattice vectors $(\frac{2\pi}{|a|}, \frac{2\pi}{|b|})$, where a and b are the real lattice vectors. 64
- 4.3 (a) CBs of $\text{K}_3\text{Ta}_3\text{B}_2\text{O}_{12}$ around the Γ point projected over z -component of spin direction. (b) Spin splitting energies (δE) of $\text{K}_3\text{Ta}_3\text{B}_2\text{O}_{12}$ (CBM), KTaGe_3O_9 (VBM) and $\text{Sr}_7\text{Br}_2\text{H}_{12}$ (VBM). Band structure and δE are plotted along $(\frac{2\pi}{a}0.14, \frac{2\pi}{b}0.14)-(0, 0)-(\frac{2\pi}{a}$ direction of the momentum space, which is along $\text{K(H)}-\Gamma(\text{A})-\text{K(M)}$ direction. The δE defines the energy different between spin-up and spin-down bands. 68
- 4.4 Spin textures of the CBs for $\text{K}_3\text{Ta}_3\text{B}_2\text{O}_{12}$ around the Γ point obtained by DFT [(a)-(b)] and $\mathbf{k}\cdot\mathbf{p}$ model [(c)-(d)]. Our spin textures are prepared using the convention [(a)-(d) as examples] that the energy of the outer branch is smaller or equal as compared to the energy of inner branch at any (k_x, k_y) point in the considered range. (e) Constant energy contours projected over the spin components having energy of $E_F + 2.38$ eV. Here, the red and blue dots denote the spins in the state $|\uparrow\rangle$ and $|\downarrow\rangle$, respectively. (f) The calculated values of Θ for spin textures of $\text{K}_3\text{Ta}_3\text{B}_2\text{O}_{12}$, KTaGe_3O_9 and $\text{Sr}_7\text{Br}_2\text{H}_{12}$ 69

- 4.5 Crystal structures of (a) α_1 - WA_2Z_4 and (b) α_2 - WA_2Z_4 monolayers with symmetry operations highlighted using red dashed line. The solid black lines indicate the corresponding unit cell. (c) The first BZ and k -points (Γ , M, K and K') are shown using red circles. (d) The phonon band dispersions of α_2 - WSi_2N_4 monolayer. (e) Variation of total energy and temperature for α_2 - WSi_2N_4 monolayer during AIMD simulation for 3 ps at 300 K. (f) Planar average of the electrostatic potential energy of the α_2 - WSi_2N_4 monolayer as a function of out-of-plane axis. 74
- 4.6 (a) Orbital-resolved electronic band structure of α_2 - WSi_2N_4 monolayer without including SOC. Symbol size is proportional to the particular orbital weightage. The constant energy contours of (b) topmost VB and (c) lowest CB in the momentum-space. The white hexagon is the first BZ. (d) Spin-resolved electronic band structure of α_2 - WSi_2N_4 monolayer. The color bar shows the x -, y - and z - components of spin polarization. 75
- 4.7 The spin splitting ($\Delta E = |E(k, \uparrow) - E(k, \downarrow)|$) of (a) topmost VB and (b) lowest CB mapped over the full BZ. 78
- 4.8 The spin textures of topmost VBs associated with the outer branch using (a) DFT and (b) $k \cdot p$ models. The energy of the outer branch is smaller or equal as compared to the energy of inner branch at the k -point in the considered range. (c) Schematic diagram of PSH state. The L_{PSH} represents the wavelength of spatially periodic mode. The band structure of topmost VBs around (d) Γ , (e) M, and (f) K points. Here, the black solid lines and red dots represent the band structure computed using DFT and $k \cdot p$ models, respectively. 79

- 4.9 (a) Side view of the bulk crystal structure of WSi_2N_4 with site point group of W atom. The red dot represents the inversion center. The two boxed real-space sectors forming the inversion partners are used for spin projection are considered as α -sector and β -sector. The black arrows on W atoms represent the direction of dipole moment on particular atomic sites. (b) The spin-projected top VBs of bulk WSi_2N_4 , bilayer (2L) and trilayer (3L). The color bar shows the out-of-plane (z -) component of spin textures. (c) The spin- and atom- projected band structure of top VBs along K-M-K path. The green and orange color shows the band is coming from α - and β -sectors, respectively. The up and down arrows shows the z -component of spin polarization. Note that the in-plane (S_x, S_y) spin components are zero along that path. 83
- 5.1 (a) Side and top views of lattice structure corresponding to monolayer H-BB WSiGeZ_4 . (b) Side views of various stacking orders for three constituent parts in the monolayer WSiGeZ_4 . The 3D view of the top valence band (VB) and bottom conduction band (CB) in monolayer (c) H-BB WSiGeN_4 and (d) H-AA WSiGeP_4 89
- 5.2 The spin resolved band structure of monolayer (a) H-BB WSiGeN_4 , (b) H-AA WSiGeP_4 and (c) H-AA WSiGeAs_4 calculated using PBE+SOC. The energy levels with positive and negative spin magnetization are sketched in the red and blue curves, respectively. (d) Schematic of valley selective excitation. Length of arrows and circles depict the energy and chirality of incident photon, respectively. 92
- 5.3 The degree of circular polarization for transition between VB to CB in monolayer (a) H-BB WSiGeN_4 and (b) H-AA WSiGeP_4 mapped over the BZ. (c) The circular polarization for transition between VB to SUCB in monolayer H-AA WSiGeP_4 . The black dotted lines represents the first BZ. 92
- 5.4 Orbital projected band structure of monolayer H-BB WSiGeN_4 without SOC. Fermi level is set to zero in the energy axis. The fatness of band structure corresponds to $W-d_{z^2}$ (green), $W-d_{x^2-y^2}$ and $W-d_{xy}$ (red), $W-d_{yz}$ and $W-d_{xz}$ (blue), and N- p (cyan) orbitals. 94
- 5.5 The variation of spin splitting of the VB and CB at K/K' valleys with respect to the biaxial strain in monolayer (a) H-BB WSiGeN_4 and (b) H-AA WSiGeP_4 96

- 5.6 Berry curvature distribution over BZ for (a) VB, (b) CB in monolayer H-BB WSiGeN₄. Berry curvature distribution of (c) VB, (d) CB and (e) SUCB in monolayer H-AA WSiGeP₄. The black dotted lines denote the first BZ. 96
- 5.7 Modulation of Berry curvature by varying stacking orders in monolayer (a) WSiGeN₄ and (b) WSiGeP₄. The insets in (a) and (b) show the position of Berry curvature at K' point. The effect of biaxial strain on the Berry curvature in monolayer (c) H-BB WSiGeN₄ and (d) H-AA WSiGeP₄. 99
- 5.8 (a) The spin-projected band structures and (b) associated spin texture of top VBs in H-AA WSiGeP₄. (c) The spin-projected band structure of top VBs in H-BA WSiGeP₄. (d) The variation of Rashba coefficients under the application of biaxial strain. 100
- 5.9 (a) The variation of Rashba coefficient (α_R) under the application of out-of-plane EEF. Zeeman spin splittings at K/K' points as a function of EEF in monolayer (b) H-BB WSiGeN₄ and (c) H-AA WSiGeP₄. Modulation of band gaps with strain in monolayer (d) H-BB WSiGeN₄, (e) H-AA WSiGeP₄ and (f) H-AA WSiGeAs₄. 100
- 5.10 (a) Top and [(b),(c)] side views of monolayer MoSi₂N₄. The x , y , and z axes are shown in each case. a_1 and a_2 are the hexagonal lattice vectors, while a'_1 and a'_2 are lattice vectors of the orthorhombic cell. The rotated Cartesian frame for strain along an arbitrary direction is shown using green lines. After applying strain along x' direction and allowing relaxation along perpendicular y' direction, the orthorhombic unit cell is shown using red dashed lines. The effect of strain on the strained lattice is exaggerated for clear illustration and is much smaller for our considered range. x and y directions are zigzag (ZZ) and armchair (AC), respectively. The atomic arrangement is ZZ along 0°, 60° and 120°, whereas AC along 30°, 90° and 150° directions. The first (d) hexagonal and (e) orthorhombic BZ are shown. M_{xy} and M_{yz} are the mirror planes, and C_{3z} is the three-fold rotation axis. The high symmetry points Γ , M, and K of hexagonal BZ are mapped in the orthorhombic BZ (see Eq. 5.9). 105

- 5.11 (a) Spin-projected band structures of the monolayer MoSi_2N_4 in the presence of SOC. (b) Evolution of band structures under the uniaxial strain of strength 4% and 8% along the ZZ and AC directions. The red arrows represent the valley drifts. (c) and (d) are the zoomed versions of low CBs and top VBs of monolayer MoSi_2N_4 with 1% uniaxial stain, respectively. The vertical dashes represent the location of energy extreme in k -space 107
- 5.12 (a) Contour plot showing isoenergy contours of the VB around the K point for the unstrained case (0%) and with the uniaxial strain of 4% along AC, IM, and ZZ directions of monolayer MoSi_2N_4 . Black arrows show the directions of valley drifts. (b) The same as in (a) for the CB. (c) Momentum drift of the CB and VB near the K point. Valley extremum as a function of uniaxial strain applied along the AC, IM, and ZZ direction. Note that only the k_x component of drift along $\text{K} \rightarrow \text{X}$, $\cos(30^\circ)$ of the net drift is shown in (c) for the IM case. The k_y component ($\sin(30^\circ)$ of the net drift) is also there and duly considered in all the calculations. The variation of (d) Young's modulus, (e) Poisson ratio, (f) direct and indirect band gap as a function of strain. 109
- 5.13 The real part of the wavefunction of (a) VB and (b) CB at the K point for monolayer MoSi_2N_4 without strain. Note that in (a) and (b), we show only the Mo- N_2 network since the contribution coming from the upper and lower Si-N layer is almost zero. The charge density difference between the unstrained and 4% strained lattice along the (c) AC and (d) ZZ directions. The electron accumulation is shown in cyan, and electron depletion is shown in yellow. . . . 112
- 5.14 (a) Berry curvature distribution summed for all VBs along the path $\text{X}'\text{-K}'\text{-}\Gamma\text{-K-X}$ in monolayer MoSi_2N_4 . Inset in (a) shows the mapping of Berry curvature under first BZ. (b) The degree of circular polarization of excitation from VB to CB at the K point. Inset in (b) shows the mapping of the degree of circular polarization in the first BZ. 113

- 6.1 Geometric structures of bilayer MnSe with high-symmetry stackings (a) AA and (b) AA'. The upper layer in AA and AA' is obtained by the translation ($d\hat{z}$) and mirror reflection (M_z) of the lower layer, respectively. The energy distribution of different translations between layers for the (c) AA and (d) AA' stacking. The energy surfaces are interpolated using 10 steps in \mathbf{a} and \mathbf{b} directions such that all possible high-symmetry stackings are included. (e) Structure of the global ground state with AB stacking having magnetization $M\uparrow\downarrow\uparrow\downarrow$. The sublayers α_i and β_i ($i = 1, 2$) are connected by $\hat{P}\hat{T}$ -center with orange dashed lines. (f) Energy band dispersion of monolayer MnSe without (solid black lines) and with an electric field (red dashed lines) of 0.05 V\AA^{-1} along z -direction. 119
- 6.2 Schematic illustration of band structures with (a) null spin splitting and (b) Zeeman spin splitting. (c) Sketches of twofold degenerate bands in the presence of $\hat{P}\hat{T}$ symmetry with hidden spin polarization, where each band is segregated on different sublayers. (d) The lifting of band degeneracy when an electric field along the z -direction is applied. The energy levels with positive and negative spin magnetization are sketched in the red and blue curves, respectively. 121
- 6.3 (a) Orbital-projected band dispersion curves of bilayer MnSe with AB stacking. (b) $|\psi_{n\mathbf{k}}(\mathbf{r})|^2$ for the states CB, CB+1, CB+2, and CB+3 at K point. Layer-projected CBs of bilayer MnSe around the K point along the (c) K- Γ and (d) K-M. (e)-(f) counterparts of (c)-(d) in the presence of a small electric field of 4 mV\AA^{-1} along the z -direction. 123
- 6.4 Spin textures of four lowermost conduction bands CB, CB+1, CB+2, and CB+3 around the K point. 125
- 6.5 The Zeeman spin splittings for the CBs (a) Δ_1 , Δ_2 and (b) Δ_α , Δ_β in bilayer MnSe as a function of electric field \mathcal{E}_z 126
- 6.6 Layer-projected CBs around K point in bilayer MnSe (a) without and with \mathcal{E}_z of strength 4 mV\AA^{-1} along (b) $+z$ and (c) $-z$ direction, respectively. Here α and β represent upper and lower layer, respectively. 126

- 6.7 The Moiré superlattices formed by twisting bilayer of MnPSe₃ [(a),(b)] and MnSe [(c),(d)] by 21.79°. Violet, brown, and green atoms represent Mn, P, and Se, respectively. The ground-state magnetic structures are also highlighted in (a) and (c). The structures are illustrated using VESTA [3]. (e) The Moiré BZ construction uses BZs of the top and bottom layers. The large red and blue hexagons are the first BZ of the top and bottom layers, respectively, and black hexagons represent the BZ corresponding to the Moiré superlattice. Spin-polarized band structure of (f) tb-MnPSe₃ and (g) tb-MnSe at the PBE level. 128
- 6.8 (a) Spin splitting energy [$\delta E = E_{\uparrow}(\mathbf{k}) - E_{\downarrow}(\mathbf{k})$] distribution of VB in 21.79° tb-MnSe. The units of k_x and k_y are Å⁻¹. CBs of tb-MnSe along the (b) K_1 - K_c - K_2 and (c) M_1 - M_c - M_2 paths [see Fig 6.7(e) for paths]. VBs of tb-MnPSe₃ along the (d) K_1 - K_c - K_2 and (e) M_1 - M_c - M_2 paths. Black dashed squares represent prominent spin splittings. 130
- 6.9 Band structures of tb-MnPSe₃ around (a) K_c and (b) M_c along q_y direction. (c) and (d) are counterparts of (a) and (b), respectively, obtained for tb-MnSe. The solid and dotted lines are band structures obtained by DFT and the model described by Eq. 6.5, respectively. 131
- 6.10 Band structures of 21.79° (a) tb-MnPSe₃ and (b) tb-MnSe in the presence of the out-of-plane electric field (\mathcal{E}_z) of strength 10 MV/cm. (c) The Zeeman spin splittings in the CB (Δ_C) and VB (Δ_V) of 21.79° tb-MnPSe₃ and tb-MnSe at Γ point as a function of \mathcal{E}_z . (d) The variation in α (see Eq. 6.5) as a function of biaxial strain for 21.79° tb-MnPSe₃ and tb-MnSe. 133

List of Tables

2.1	The transformations of the \mathbf{k} and (σ) Pauli matrices under the operations belonging to C_{2v} point group. The symbol K represents complex conjugation.	38
3.1	Lattice parameters and polarization for rhombohedral phases of KIO calculated using PBE ϵ_{xc} functional.	44
3.2	Rashba parameters for band-splitting at k -point A for $R3m$ phase (note that $\beta=-\alpha$ in each case).	48
3.3	Rashba parameters for band-splitting at k -point Γ for $R3c$ phase.	51
3.4	Calculated lattice parameters of $\text{Sn}_2\text{SbX}_2\text{I}_3$ ($X = \text{S}, \text{Se}$). The experimental values are provided from Ref. [4] for comparison.	55
3.5	The transformation rules of (k_x, k_y, k_z) and $(\sigma_x, \sigma_y, \sigma_z)$ under the operations belonging to the group of wave vector of Y point and time reversal operation (T). The \mathbf{k} is referenced from the Y point.	57
3.6	The parameterization of $\alpha_{(1)}, \alpha_{(3)}, \beta_{(1)}, \beta_{(3)}, \gamma_\alpha$ and γ_β for the lowest CBs and top VBs (around the Y point) of $\text{Sn}_2\text{SbS}_2\text{I}_3$ having $Cmc2_1$ group symmetry. The k_x and k_y ranges considered to fit our models are within 0.125 \AA^{-1}	58
4.1	The transformations of $(\sigma_x, \sigma_y, \sigma_z)$ and (k_x, k_y, k_z) under the generators of the C_{2v}, D_{3h} , and C_{3h} point group and time-reversal operator (T). The first row shows the point group operations and the corresponding point group symmetries. The last row shows the symmetry invariant terms. Note that we have included the terms upto cubic in \mathbf{k} and higher order contributions are found to be insignificant.	66
4.2	The materials showing PCS with PST along with their parameters of Equation 4.11. The splitting is observed for lower CBs (CB) or higher VBs (VB) around the high-symmetry-points (HSP) Γ and A.	71

4.3	Optimized lattice constant ($a = b$) of the unitcell of WA_2Z_4 monolayers. The calculated formation energy per atom (E_{for}), dipole moment per unit cell (P_y), band gaps without and with SOC using PBE (E_g^{PBE} , $E_g^{PBE+SOC}$) and HSE06 ($E_g^{HSE+SOC}$, $E_g^{HSE+SOC}$). The calculated band gaps using G_0W_0 performed on top of PBE functional with inclusion of SOC (E_g^{GW}).	76
4.4	The calculated SOC parameters, viz. α , Δ and wavelength of PSH mode (L_{PSH}) of upper VBs for WA_2Z_4 family.	82
5.1	Optimized lattice constant (a) for the unit cell of $WSiGeZ_4$ monolayer. The calculated formation energy per atom (E_{for}), dipole moment per unit cell (P_y , P_z), band gaps in presence of SOC using PBE (E_g^{PBE}) and HSE06 (E_g^{HSE}). The calculated band gaps using G_0W_0 performed on top of PBE functional with inclusion of SOC ($E_g^{GW@PBE}$).	90
5.2	The observed spin splitting of VB (ΔE_K^{VB}), CB (ΔE_K^{CB}), SUCB (ΔE_K^{SUCB}) and the Berry curvature (Ω_K) at K point.	95
5.3	Orbital contribution to the VB at K/K' point of monolayer H-AA $WSiGeP_4$	99
5.4	The calculated parameters (E_R , k_R and α_R) for Rashba spin splitting around Γ point.	102
5.5	The acoustic phonon limited carrier mobility and other relevant parameters for $WSiGeZ_4$ monolayer. The x and y directions correspond to armchair and zigzag directions, respectively. m_o is rest mass of the electron.	102
5.6	The irreducible representations and basis functions for the little group C_{3h} ($= C_3 \times \sigma_h$) of K/K' point [5]. The sign \pm corresponds to $\pm K$ points. The last column contains the energy bands to which basis functions contribute.	111
6.1	The transformation rules of electric polarization (P_x , P_y , P_z) and Pauli spin matrices ($\hat{\sigma}_x$, $\hat{\sigma}_y$, $\hat{\sigma}_z$) with respect to operation (\hat{O}) belonging to MPG $2'/m$	122
6.2	Classification of 2D materials based on the MSG type, magnetic order and their impact on the nonrelativistic spin splitting. Here, \hat{P} , \hat{T} , \hat{M}_{xy} , \hat{U} , and $\hat{\tau}$ represent inversion, time-reversal, planar mirror, spinor, and translation symmetry, respectively. The relevant symmetry is also indicated in the case of spin-degeneracy at generic k	132